International Journal of Nanomedicine

Dovepress
open access to scientific and medical research

Open Access Full Text Article

ORIGINAL RESEARCH

Development and Preclinical Evaluation of a Near-Infrared Fluorescence Probe Based on Tailored Hepatitis B Core Particles for Imaging-Guided Surgery in Breast Cancer

Rui-Qin Yang[1–3], Min Chen[3,4], Qiang Zhang[5], Yi-Yang Gao[1–3], Kang-Liang Lou[1–3], Tong-Tong Lin[5], Wen-He Huang[1,2], Yun-Zhu Zeng[6], Yong-Qu Zhang[1–3], Yong-Ying Dang[1–3], Lei Ren[5]*, Guo-Jun Zhang[1,2,4]*

[1]Cancer Center & Department of Breast and Thyroid Surgery, Xiang'an Hospital of Xiamen University, School of Medicine, Xiamen University, Xiamen, Fujian, People's Republic of China; [2]Key Laboratory for Endocrine-Related Cancer Precision Medicine of Xiamen, Xiang'an Hospital of Xiamen University, Xiamen, Fujian, People's Republic of China; [3]Clinical Central Research Core, Xiang'an Hospital of Xiamen University, Xiamen, Fujian, People's Republic of China; [4]Cancer Research Center, School of Medicine, Xiamen University, Xiamen, Fujian, People's Republic of China; [5]State Key Lab of Physical Chemistry of Solid Surface, College of Materials, Xiamen University, Xiamen, Fujian, People's Republic of China; [6]The Pathology department, Cancer Hospital, Shantou University Medical College, Shantou, Guangdong, People's Republic of China

*These authors contributed equally to this work

Correspondence: Guo-Jun Zhang, Tel +86-592-2889988, Fax +86-592-2889202, Email gjzhang@xah.xmu.edu.cn

Purpose: Tumor-free surgical margin is crucial but challenging in breast-conserving surgery (BCS). Fluorescence imaging is a promising strategy for surgical navigation that can reliably assist the surgeon with visualization Of the tumor in real-time. Notably, finding an optimized fluorescent probe has been a challenging research topic. Herein, we developed a novel near-infrared (NIR) fluorescent probe based on tailored Hepatitis B Core virus-like protein (HBc VLP) and presented the preclinical imaging-guided surgery.

Methods: The RGD-HBc_{160} VLP was synthesized by genetic engineering followed encapsulation of ICG via disassembly-reassembly. The applicability of the probe was tested for cell and tissue binding capacities through cell-based plate assays, xenograft mice model, and MMTV-PyVT mammary tumor transgenic mice. Subsequently, the efficacy of RGD-HBc_{160}/ICG-guided surgery was evaluated in an infiltrative tumor-bearing mouse model. The protein-induced body's immune response was further assessed.

Results: The prepared RGD-HBc_{160}/ICG showed outstanding integrin $\alpha_v\beta_3$ targeting ability in vitro and in vivo. After intravenous administration of probe, the fluorescence guidance facilitated more complete tumor resection and improved overall survival Of the infiltrative tumor-bearing mice. The probe also showed the excellent capability to differentiate between benign and malignant breast tissues in the mammary tumor transgenic mice. Interestingly, the ingenious tailoring of HBc VLP could not only endow its tumor-targeting ability towards integrin $\alpha_v\beta_3$ but also significantly reduce the humoral and cellular immune response.

Conclusion: The RGD-HBc_{160}/ICG holds promise as an effective tool to delineate tumor margin. These results have translational potential to achieve margin-negative resection and improve the stratification of patients for a potentially curative.

Keywords: breast Cancer, tumor margin, NIR fluorescence imaging, imaging-guided surgery, Hepatitis B core virus-like particles

Introduction

According to global cancer statistics, as of 2020, breast cancer was the most commonly diagnosed cancer and the leading cause of cancer death in women.[1] Breast-conserving surgery (BCS) plus adjuvant radiation therapy remains a standard therapeutic modality for early-stage breast cancer.[2] As incomplete resections are associated with higher recurrence rates and shorter overall survival, tumor-free surgical margins are critical in BCS.[3,4] However, intraoperative identification of

Received: 9 October 2021
Accepted: 11 January 2022
Published: 22 March 2022

Graphical Abstract

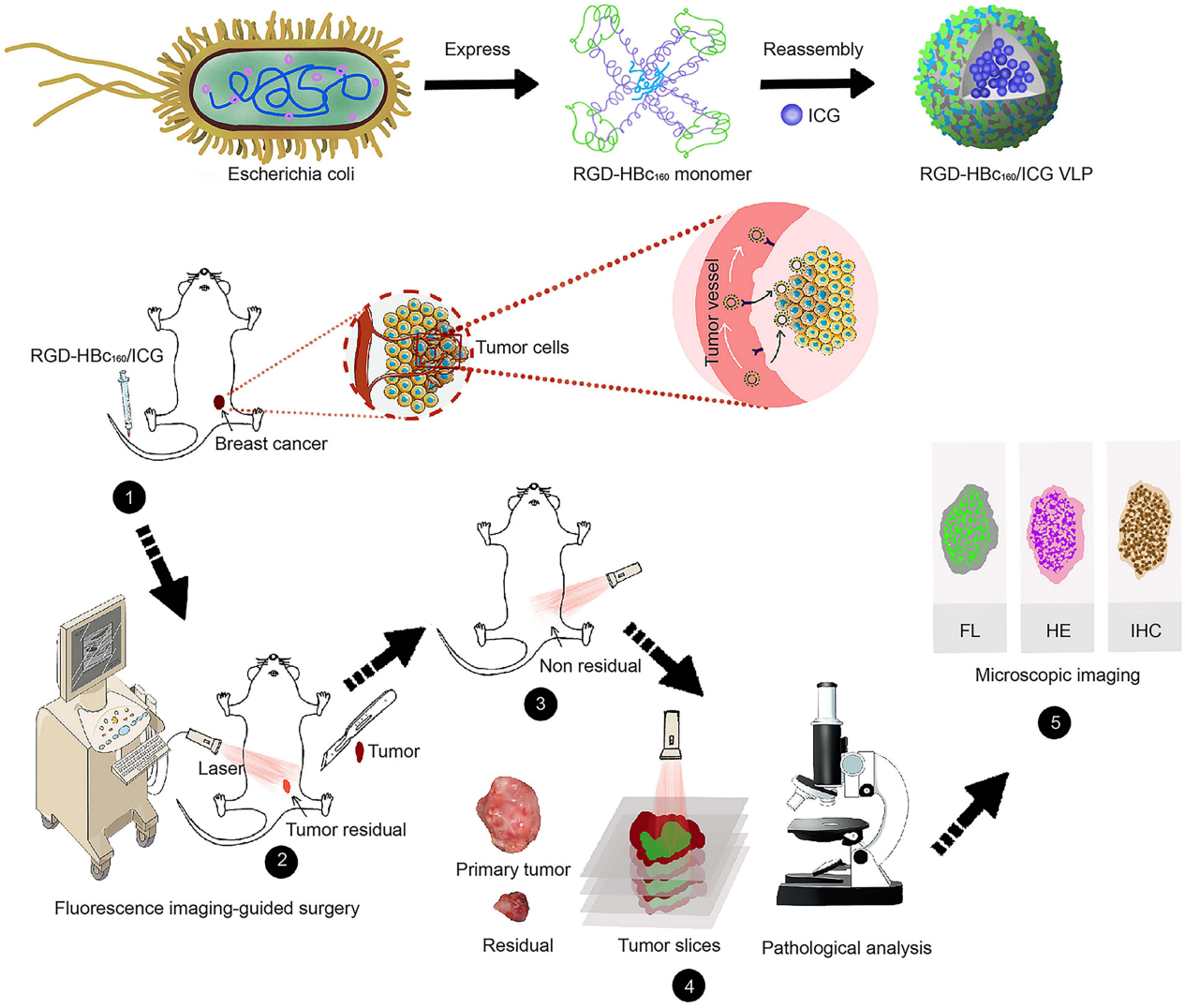

tumor boundaries mainly relies on subjective visual inspection and palpation, and positive margins are found in 20 to 55% of cases.[5] Intraoperative frozen-section analysis are time-consuming and low sensitivity,[6] while other conventional imaging techniques, such as computed tomography and magnetic resonance imaging, are generally difficult to integrate into the operating room.[7] Most importantly, these conventional imaging modalities cannot reliably communicate real-time feedback to the surgeon and have limited tumor specificity. Thus, it is imperative to develop intraoperative imaging techniques to accurately delineate tumor margin.

In response to this pressing clinical challenge, fluorescence imaging-guided surgery has emerged as a promising strategy that uses fluorescence to highlight tumor tissue. More specifically, this modality allows for labeling at the molecular-cellular level, thus achieving superior resolution and sensitivity compared to conventional anatomical imaging.[8–10] Furthermore, with the advantages of deep penetration and low background fluorescence, Near-infrared (NIR) imaging (also called biological transparent window imaging[11,12]) is more suitable for in vivo imaging. Currently, the FDA-approved NIR dye ICG is widely used in guiding resection of malignancies such as hepatobiliary cancer,[13] detecting sentinel lymph nodes,[14–16] and conserving organ function.[17] However, in current fluorescence image-guided

surgery practice, free ICG normally experienced short-time tumor retention because of their rapid clearance and shows poor tumor-to-background ratio (TBR) in vivo. Furthermore, due to the lack of tumor targeting of ICG, the sensitivity and specificity for delineating tumor margins are insufficient.[18,19] Therefore, overcome the above shortcomings of ICG are the prerequisite to intraoperatively precisely differentiate the tumor and normal tissue in real-time.

Organic nanoparticles, which can be adapted to have various biological properties for use in a range of settings, can provide a safer and more effective delivery platform,[20] and are gradually being applied in clinical practice.[21,22] Notably, natural protein subunits-based nanoparticles with the advantages of biocompatibility and biodegradation as compared to synthetic nanoparticles.[23,24] In particular, among numerous protein-based nanoparticles, Hepatitis B Core virus-like particles (HBc VLPs) possess features of flexibility for tailoring and capacity of self-assemble, which attracted a great of attention for the bioimaging.[25] Unfortunately, natural HBc VLP lacks tumor-targeting properties and could induce the strong in vivo immune responses.[26]

In the present study, we inserted RGD sequence into the main immune region (MIR) of HBc protein, and the amino acids in B cell and Cytotoxic T lymphocyte (CTL) epitope were substituted by non-function ones. On the one hand, the RGD peptide is an affinity ligand of integrin $\alpha_v\beta_3$, which is a Surface membrane protein involved in tumor angiogenesis that is frequently overexpressed in breast cancer,[27] and on the other hand, which can disrupt the immune region, thus attenuate recognition by the immune system. Based on this innovative targeting platform, we encapsulated ICG within the core of HBc VLP to develop a novel NIR fluorescent probe and evaluated specific targeting in breast cancer cells and several breast cancer mouse models, including subcutaneous and transgenic mouse mammary tumors, aiming to further expand the palette of NIR contrast agents available to guide the BCS. Finally, the clinical translation potential of RGD-HBc_{160}/ICG to provide surgical guidance, and thereby reduce the incidence of positive surgical margins, was evaluated.

Materials and Methods

Preparation of the RGD-HBc_{160} and Synthesis of the Probe

By means of gene design, we inserted glycine-rich RGD sequence on the surface (between residues 78 and 81) of the HBc_{183}, and the amino acids in B cell and CTL epitope were substituted by non-function ones, the redundant amino acids on the C-terminus of the HBc monomer which is not related to the structure assembly were eliminated to constructed RGD-HBc_{160}. The peptide sequence of the HBc_{183} and RGD-HBc_{16} were presented in Data S1. Subsequently, the plasmid pET43.1(a)-RGD-HBc160 was customized from Shanghai Generay Biotech Co. Ltd, and then transformed into E. coli BL21 (DE3) for protein expression. The protocol of protein expression and purification was according to the previous report.[25] The recombinant RGD-HBc_{160} VLPs were reversibly disassembled with depolymerizing buffer. After the disassembly, ICG was added into the protein solution with a mass ratio of 1:10 and the solution was intermittently stirred at 4°C for 30 min. Reassembly of RGD-HBc_{160}/ICG was then conducted by dialysis in an assembling buffer overnight and free ICG was removed throughout this procedure.

Characterization of RGD-HBc_{160}/ICG

The absorption spectra and fluorescence emission spectra of the RGD-HBc_{160}/ICG were measured by full wavelength multifunctional microplate reader (Varioskan Flash) and the fluorescence spectrometer (Varian Eclipse), respectively. The morphology and diameter distribution of RGD-HBc_{160}/ICG were observed by a JEM-1400 TEM (100 kV). A Horiba instrument was used to measure the mean hydrodynamic diameter (HORIBA SZ-100, Japan). All measurements were performed at 25°C. Moreover, to evaluate the RGD-HBc_{160}/ICG stabilities in different medium (PBS, 10% fetal bovine serum (FBS), water and DMEM Cell culture medium), samples were stored in the dark at 25 °C for 96 h. At selected time points, hydrodynamic diameter and fluorescence emission spectra were measured, respectively, for the corresponding solutions.

Cell Culture and Flow Cytometry

The human breast cancer cell line MDA-MB-231 and non-cancerous mammary epithelial cell line MCF-10A cells were obtained from the American Type Culture Collection (Rockville, USA), MDA-MB-231-luc was obtained from the Hon

sun Biological Technology Co, Ltd, China. MDA-MB-231 and MDA-MB-231-luc cells were maintained in DMEM medium containing 10% FBS, 1% penicillin and streptomycin. MCF-10A cells were maintained in Mammary Epithelial Cell Growth Medium Bullet Kit Clonetics™ (Lonza, CC-3150, Alpharetta, GA, USA). In the flow cytometry experiments, the MDA-MB-231, and MCF-10A cells were placed in a 6-well chamber and further cultured for 24 h, then detached with trypsin/EDTA. Subsequently, the cells were incubated with anti-$\alpha_v\beta_3$ rabbit mAb (bs-1310R, Bioss, 1:100) for 2 hours. Whereafter, cells were washed thrice and incubated with the secondary antibody (ab150077, Abcam, 1:1000) for 30 min. Lastly, the cells were washed thrice with the buffer, and then analyzed by the flow cytometer (CytoFlexS, Beckman).

Cytotoxicity Assay

MDA-MB-231 and MCF-10A cells (5 * 10^3 cells/well) were seeded in 96-well plates and incubated for 12 h. Then, the cell medium was replaced with fresh culture medium containing varying concentrations of RGD-HBc_{160}/ICG (0, 25, 50, 100, and 200 μg/mL). After 48 h, determining the cell viability by CCK-8 assay (Beyotime Biotechnology).

Cellular Uptake Study

MDA-MB-231 and MCF-10A were placed in a 12-well chamber slide at 1 * 10^5 cells per well and maintained for 24 h. Subsequently, the cells were treated with different concentrations of RGD-HBc_{160}/ICG (0, 15, 30, and 60 μg/mL). In another group, MDA-MB-231 cells were incubated with RGD-HBc_{160}/ICG, HBc_{183}/ICG, and free ICG, respectively, under the equivalent ICG concentrations (4 μg/mL). After 8 h incubation, cells were stained with DAPI (Beyotime Biotechnology). Finally, cellular uptake was observed by fluorescence microscopy (Leica DM2700 P, USA) with light cube ICG (excitation 780 to 790 nm, emission 790 to 840 nm), and light cube DAPI (excitation 357 to 344 nm, emission 447 to 460 nm). For quantitative analysis, three 40X fields were randomly selected and ICG mean fluorescence intensity (MFI) of the cells was calculated using a custom region of interest (ROI) generated for each slide by the imaging software ImageJ. Specificity of RGD-HBc_{160}/ICG binding to cells was further determined by a blocking experiment featuring treatment of MDA-MB-231 cells with c(RGDfK) (GL Biochem) (75 μg/mL) for 2 h, then added the RGD-HBc_{160}/ICG (60 μg/mL) and continue to incubate for 8 h. Subsequently, the samples were collected and analyzed as described above.

Subcutaneous Mouse Model

Animal experiments were performed in compliance with the guidelines approved by the Institutional Animal Care and Use Committee of Xiamen University. BALB/c nude mice (aged 6 to 8 weeks, Charles River Labs, China) were injected subcutaneously of the 2*10^6 MDA-MB-231 cells into the right side of the lower limbs. Bodyweight, appearance, and tumor growth were monitored every other day. The standard formula (length × $width^2$ × 0.52) was used to calculate the tumor volume.

Infiltrative Tumor Mouse Model

Total 2*10^6 MDA-MB-231-luc cells were slowly injected into the subcutaneous and superficial muscle of the posterior thigh in the right leg. Calipers were used to measure the tumor size and to monitor tumor growth.

NIR Fluorescence Imaging

The MDA-MB-231 tumor-bearing mice (volume ~300 to 400 mm^3) were randomly divided into three groups (n = 4) and injected intravenously with gradient doses of RGD-HBc_{160}/ICG (12.25, 25, 50 mg/kg), respectively. Animals were given isoflurane (RWD Life Science) for anesthesia, and the fluorescence signal was assessed by the IVIS-II imaging system (PerkinElmer) at different time points. For quantitative analysis, tumor MFIs were calculated using a custom ROI generated for the mice by the Living-Image software (PerkinElmer). The TBR was defined as the tumor MFI/MFI of normal forearm tissue. For further verification, the MDA-MB-231 tumor-bearing mice were randomly divided into three groups (n = 4) and intravenously injection of the RGD-HBc_{160}/ICG (25 mg/kg), HBc_{183}/ICG, and ICG, under the equivalent ICG dose (1.72 mg/kg). Fluorescence imaging was performed and TBRs were assessed at different time points.

Bio-Distribution in vivo and Multilevel Framework Analysis of the Fluorescent Probe

Mice bearing subcutaneous breast tumors (volume ~300 to 400 mm^3, n = 3) were injected intravenously with RGD-HBc_{160}/ICG (25 mg/kg), and mice were euthanized humanely at 36 h post-injection for collection and visualization of tumors, major organs and muscle with the IVIS-II system. For further quantitative analysis, the fluorescence intensity was calculated using the Living-Image software. Thereafter, the fresh tumors and part muscle tissues were processed further for multilevel analyses. Firstly, the formalin-fixed paraffin-embedded (FFPE) blocks and 10-μm-thick sections of both tissue samples were subjected to imaging by the fluorescence flatbed scanning system (LI-COR Biosciences Inc.). Afterward, we performed hematoxylin/eosin (H/E) staining to enable the direct correlation between fluorescence signal and histology on the same tissue slide. Lastly, 4-μm-thick adjacent sections from the same FFPE blocks were counter-stained with DAPI for microscopic assessment of the NIR signal at a cellular level.

Fluorescence-Guided Survival Surgery

Twenty MDA-MB-231-luc infiltrative tumor-bearing mice (~500 to 600 mm^3) were given isoflurane for anesthesia and surgical removal of the tumors was performed by visualization under white light (WL). Subsequently, 10 randomly-selected mice from the above were assessed for remaining fluorescence signals in the surgical cavity using the hand-held fluorescence imaging system. If there was residual fluorescence, further excision was performed until no residual signal remained. The residual fluorescent tissue was collected for ex-vivo fluorescence imaging and histologic analysis. The bodyweight changes and tumor recurrence of mice were monitored every other day. Any mice with tumor recurrence volume >1500 mm^3 or loss of 25% of body weight were euthanized. Bioluminescence examination was performed 15 days later.

Transgenic Mouse Model of Breast Cancer

FVB/N-Tg(MMTV-PyVT) 634Mul/J mice (PyVT) were purchased from Jackson Laboratory (Bar Harbor, ME) and crossed with wild-type FVB/N mice. Firstly, mice (n = 3, 8 weeks) with invasive mammary gland cancers and wild-type mice of the same age were injected intravenously with RGD-HBc_{160}/ICG (25 mg/kg). After 36 h, immediately before imaging, the mice were humanely euthanized and 4–5th of the mammary glands were sequentially resected and imaging was performed to simulate a step-wise surgical resection with imaging guidance. Fluorescence imaging were performed before and after removal of each sequential quarter (n = 24) of the combined fourth and fifth mammary glands in each group. Ex-vivo imaging of resected tissues was conducted via the IVIS-II imaging platform, and the tissues were subsequently conducted histopathological analysis. Lastly, ex vivo fluorescence intensity of tumor specimens from two groups was calculated.

To further assess the ability of the probe to identify malignant tissues, transgenic mice (n = 6) between the ages of 5 and 8 weeks with mammary disease stages ranging from normal to invasive cancers received intravenous injection of the RGD-HBc_{160}/ICG (25 mg/kg). After 36 h, the fourth and fifth mammary glands were divided into four segments (on average) for fluorescence imaging on the IVIS imaging platform followed by histopathological assessment. All of the tissues were embedded in paraffin blocks and sections (10-μm-thick) were then imaged using a fluorescence flatbed scanning system (Odyssey® CLX). Then, adjacent 4-μm sections were made for H/E staining to evaluate the correlation between fluorescence signal and histology in each section. All of the slides were reviewed by a pathologist who specializes in breast cancer and a receiver operator characteristic (ROC) curve was fitted by the fluorescence intensity and the pathological findings in fresh tissue specimens. In addition, microsegments of FFPE sections (10-μm-thick) were made to determine the biodistribution of the RGD-HBc_{160}/ICG in the transgenic mouse breast tissues. Tumor characteristics (invasive tumor, tumor in situ) and components of healthy parenchymal tissue, including collagen, normal breast ductal tissue, fat, and fat tissues, were identified and delineated manually on the digitalized H/E slides, and the delineated tissue components were then examined by fluorescence quantitative analysis using the CLX fluorescence platform.

Immunization Protocol

Female BALB/c mice (4–6 weeks) were randomly divided into three groups (n = 3) and 200 μg of HBc_{183}, RGD-HBc_{160}, PBS were injected intravenously twice base with a one-week interval between injections, respectively. Mice were euthanized humanely for the collection of spleen tissues and blood samples 7 days after the second immunization. Lymphocytes from the spleen tissues were separated with kits (P8860, Solarbio Life Sciences), and then stained with anti-CD3-APC, anti-CD4-FITC, and anti-CD8-PE antibodies according to the manufacturer's protocols (Thermo Fisher Scientific) for flow cytometric analysis. γ-IFN and TNF-α cytokine concentrations in the serum were analyzed with Mouse ELISA Kits according to the manufacturer's instructions (7324–88, 7064–88, Thermo Fisher Scientific). Lastly, we performed the enzyme-linked immune sorbent assay (ELISA) to detection the serum specific antibody, as mentioned elsewhere,[28] the serum was diluted $1/10^5$, the absorption at 450 nm was read on a spectrophotometer.

Safety Study

The biosafety of RGD-HBc_{160}/ICG was assessed in healthy BALB/c mice. After injection with 25 mg/kg RGD-HBc_{160}/ICG, the weight and overall appearance of the mice were monitored for 3 weeks. Blood was collected at different time (before, 1 h, 1 day, 1 week, and 3 weeks after injection) for testing of biochemical indexes including alanine aminotransferase (ALT), aspartate aminotransferase (AST), creatinine (Cre), and blood urea nitrogen (Urea). In addition, healthy BALB/c mice were injected intravenously with 25 mg/kg RGD-HBc_{160}/ICG while mice received PBS treatment as a control group. The mice were euthanized (n = 3/time point) at 1 day, 1 week, and 3 weeks post-injection and blood was collected for testing of hemocytology indexes, major organs (heart, liver, spleen, lung, and kidney) were collected for histological analysis.

Immunohistochemical Staining for α_v Expression in Human Breast Tissues

According to a HIPPA compliant and IRB-approved protocol, resected cancer tissues from 40 breast cancers and corresponding paratumor tissues (n = 40) were obtained from the patient's resected tissue microarrays (obtained after informed consent of patients). All tissues were identified by a dedicated breast pathologist. The paraffin-embedded tissues were cut at 4 μm and immunohistochemical (IHC) staining was performed using Abcam ab179475 anti-human integrin α_v protein antibodies (1:500). All the stained sections were scored by a dedicated breast pathologist for staining intensity and percentage of positive tumor tissue. Staining intensity for α_v protein was scored as: 0 = no staining; 1 = weak; 2 = moderate; and 3 = strong tissue staining; and the percentage of positive tumor tissue in the field of view, including vessels, stroma, cytoplasm, and fibroblast like cells, was scored as: 0 = <5%; 1 = 5 to 25%; 2 = 26 to 50%; 3 = 51 to 75%; and 4 = 76 to 100%. A composite histology score was then calculated by multiplying the staining intensity score by the area covered score, giving an IHC score range from 1 to 12.

Statistical Analysis

All data were presented as means with standard deviations (SDs). Means were compared using independent samples *t*-test or with one-way ANOVA and survival was assessed by Kaplan-Meier analysis. All experiments were performed in triplicate. A *P*-value of < 0.05 was considered to indicate a significant difference. Graphing and linear regression were performed in GraphPad Prism 7.0 (IBM Corp).

Results

Synthesis and Characterization of the RGD-HBc_{160}/ICG

Transmission electron microscope (TEM) images showed that the RGD-HBc_{160}/ICG was monodispersed and spherical, and DLS analysis indicated an average hydrate particle size of 30.8 ± 2.5 nm (Figure 1A and B). RGD-HBc_{160}/ICG and free ICG exhibited similar NIR absorption and emission (Figure 1C and D). Besides, to further verify the stability of the probe in vitro, the probe was dissolved in different mediums (PBS, water and DMEM Cell culture medium) and the particle size was measured at different times. We found that the particle size of the RGD-HBc_{160}/ICG did not change significantly at 0, 4, or 96 h (Figure S1A). Moreover, the results also showed that RGD-HBc_{160}/ICG retained more than

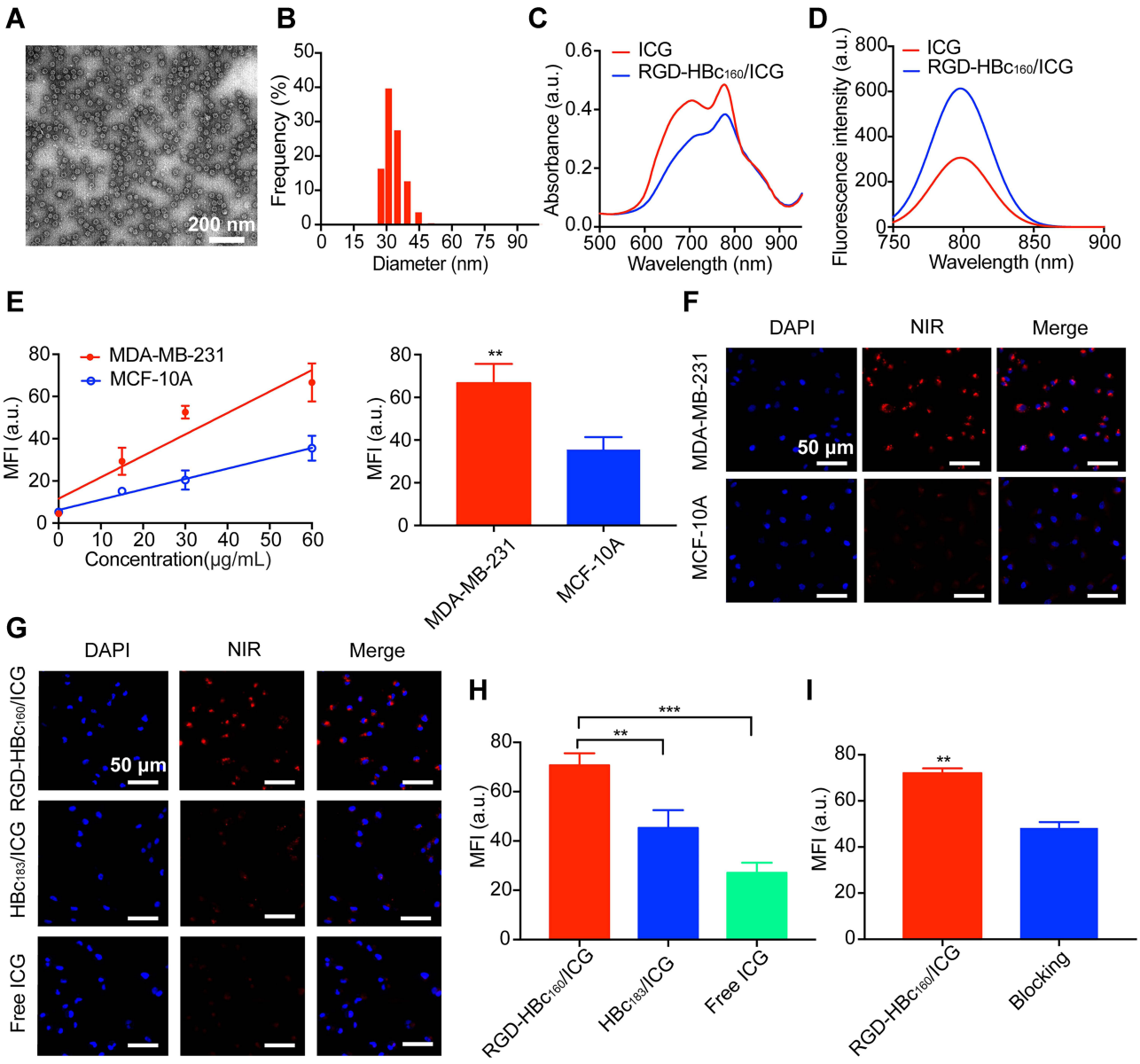

Figure 1 Characterization and cellular uptake of RGD-HBc$_{160}$/ICG. (**A**) Transmission electron microscopy images of RGD-HBc$_{160}$/ICG. (**B**) Diameter distribution of RGD-HBc$_{160}$/ICG. Representation of absorption spectra (**C**), and fluorescence emission spectra (**D**), of free ICG and RGD-HBc$_{160}$/ICG. (**E**) Representation of MFI at fluorescence microscopy in MDA-MB-231 and MCF-10A cells following incubation with different RGD-HBc$_{160}$/ICG concentrations (left), and comparison of MFI (right) at the selected concentration. (**F**) Representative fluorescence microscopy of MDA-MB-231 and MCF-10A treated with RGD-HBc$_{160}$/ICG. Representative fluorescence microscopy images from MDA-MB-231 cells after treated with RGD-HBc$_{160}$/ICG, HBc$_{183}$/ICG, and ICG (**G**), and comparison of MFI (**H**). (**I**) Comparison of MFI in MDA-MB-231 cells after incubation with RGD-HBc$_{160}$/ICG and blocking with c(RGDfK) peptides. $^{**}P<0.01$, $^{***}P<0.001$.

80% of its initial NIR fluorescence intensities in different mediums (PBS, 10% fetal bovine serum (FBS), water and DMEM Cell culture medium) at 96 h (Figures S1B). These results suggested that the RGD-HBc$_{160}$/ICG maintain the nicely fluorescence stability of ICG, which will provide greater advantages for the application of long-time intraoperative imaging. Moreover, we measured the mass ratio of protein to dyes was about 13.3:1.

Cytotoxicity Assay and $\alpha_v\beta_3$ Specificity in vitro

In cytotoxicity assay, the RGD-HBc$_{160}$/ICG showed no obvious toxicity in both MDA-MB-231 and MCF-10A cells (Figure S2). Flow cytometry analysis demonstrated that MDA-MB-231 cell lines showed higher $\alpha_v\beta_3$ expression than MCF-10A cell lines (Figure S3). Furthermore, the retained $\alpha_v\beta_3$-specificity of RGD-HBc$_{160}$/ICG was confirmed using

chamber slide assays in MDA-MB-231 and MCF-10A cell lines. As shown in Figure 1E, increasing concentrations of the RGD-HBc_{160}/ICG resulted in a linear increase in fluorescence intensity in the MDA-MB-231 cells while showing limited signal intensity change in the MCF-10A cells. Probe uptake was significantly higher in MDA-MB-231 than in MCF-10A after incubation with RGD-HBc_{160}/ICG at the same concentration (60 μg/mL) ($P<0.01$). To further verify the probe targeting specificity, the MDA-MB-231 cells were treated with RGD-HBc_{160}/ICG, HBc_{183}/ICG, and free ICG, respectively, MFI in the RGD-HBc_{160}/ICG group was higher than in the HBc_{183}/ICG and free ICG groups ($P<0.05$) (Figure 1G and H). Besides, blocking of RGD-HBc_{160}/ICG with c(RGDfK) peptides resulted in about 50% decrease of the fluorescence intensity, further supporting the $\alpha_v\beta_3$-specific target specialty of RGD-HBc_{160}/ICG (Figure 1I).

Specificity and Biodistribution of RGD-HBc_{160}/ICG in Subcutaneous Mouse Tumor Models

Firstly, we used three different doses to validate the performance of the RGD-HBc_{160}/ICG in vivo. Fluorescence imaging showed tumor fluorescent signal at different time points (Figure S4). At 36 h, higher TBRs were observed at the 25 mg/kg (TBR 5.3 ± 0.3) and 50 mg/kg (TBR 6.0 ± 0.7) doses (Figure 2A). This difference did not reach statistical significance, but the 12.25 mg/kg dose was associated with a significantly lower TBR than both the 25 mg/kg and 50 mg/kg doses at 36 h ($P<0.01$) (Figure 2B). Therefore, we adopted the 25 mg/kg dose for the subsequent experiments, and at 36 h prior to surgery, the optimal time window. To further verify the specificity of the probe in vivo, nude mice were injected with RGD-HBc_{160}/ICG (25 mg/kg), HBc_{183}/ICG, and free ICG respectively, NIR fluorescence imaging showed that in free ICG group, the fluorescence signal primarily accumulated in the liver, while only weak signal could be observed in the tumor over the prolongation of time. In contrast, the RGD-HBc_{160}/ICG group shown a strong fluorescence signal in tumor and retained up to 72 h post-injection (Figure 2C and D) and the TBR was significantly higher in the RGD-HBc_{160}/ICG group compared to the others ($P<0.05$; 5.8 ± 0.4 vs 3.1 ± 0.8 vs 2.2 ± 0.2), suggesting specific targeting of $\alpha_v\beta_3$ by RGD-HBc_{160}/ICG (Figure 2E).

Next, the bio-distribution of the probe was evaluated by posthumous examination of major organs and tumor with ex vivo fluorescence imaging, the mouse organs were dissected at 36 h post injection for fluorescence imaging, as shown in Figure 2F, the ex vivo liver showed the highest total fluorescent signals, while the tumor and kidney emitted medium fluorescent signals and other organs and tissues showed weak fluorescence. To further evaluate the correlation between the fluorescence signal with histopathology information from macroscopic to microscopic levels, we used a multilevel analytical framework. The tumor and adjacent muscle tissues were fixed in formaldehyde, embedded in paraffin blocks, and sectioned into 10-μm and 4-μm slices, and we found strong fluorescence signals in the tumor tissues but not the muscle tissues (Figure S5A). The MFI ratio of tumor to muscle was 4.8 ± 0.86 (1.8 ± 0.1 au *vs* 0.4 ± 0.07 au) at the microscopic level (Figure S5B). These results illustrate the consistency between fluorescence imaging and both macro and micro tumor imaging.

Surgical Resection of Infiltrative Tumor Under Real-Time Fluorescence Guidance

Firstly, we engrafted MDA-MB-231-luc cells part-intramuscularly into BALB/c nu mice, which produced an infiltrative tumor mouse model wherein tumor tissue was difficult to distinguish from muscle tissue. As shown in Figure 3A, no residual tumor was visible to the naked eye after a first excision under white light. However, fluorescence imaging indicated the presence of residual fluorescence in the tumor cavity, which was subsequently excised under imaging guidance until no further fluorescence was observed. Ex vivo fluorescence imaging of the excised tissue was consistent with the intraoperative imaging findings (Figure 3B), and the presence of tumor in the residual fluorescent tissues was confirmed by subsequent histopathology analysis (Figure 3C). At 15 days after the surgery, mice were assessed for local tumor residual by bioluminescence imaging. Bioluminescence was detected in 80% (8/10) mice in the white light-guided only surgery group, whereas only 20% (2/10) mice in the fluorescence-guided surgery group showed residual tumor (Figure 3D). The Kaplan-Meier survival curve (Figure 3E) indicates that the lower residual was associated with better overall survival ($P<0.05$).

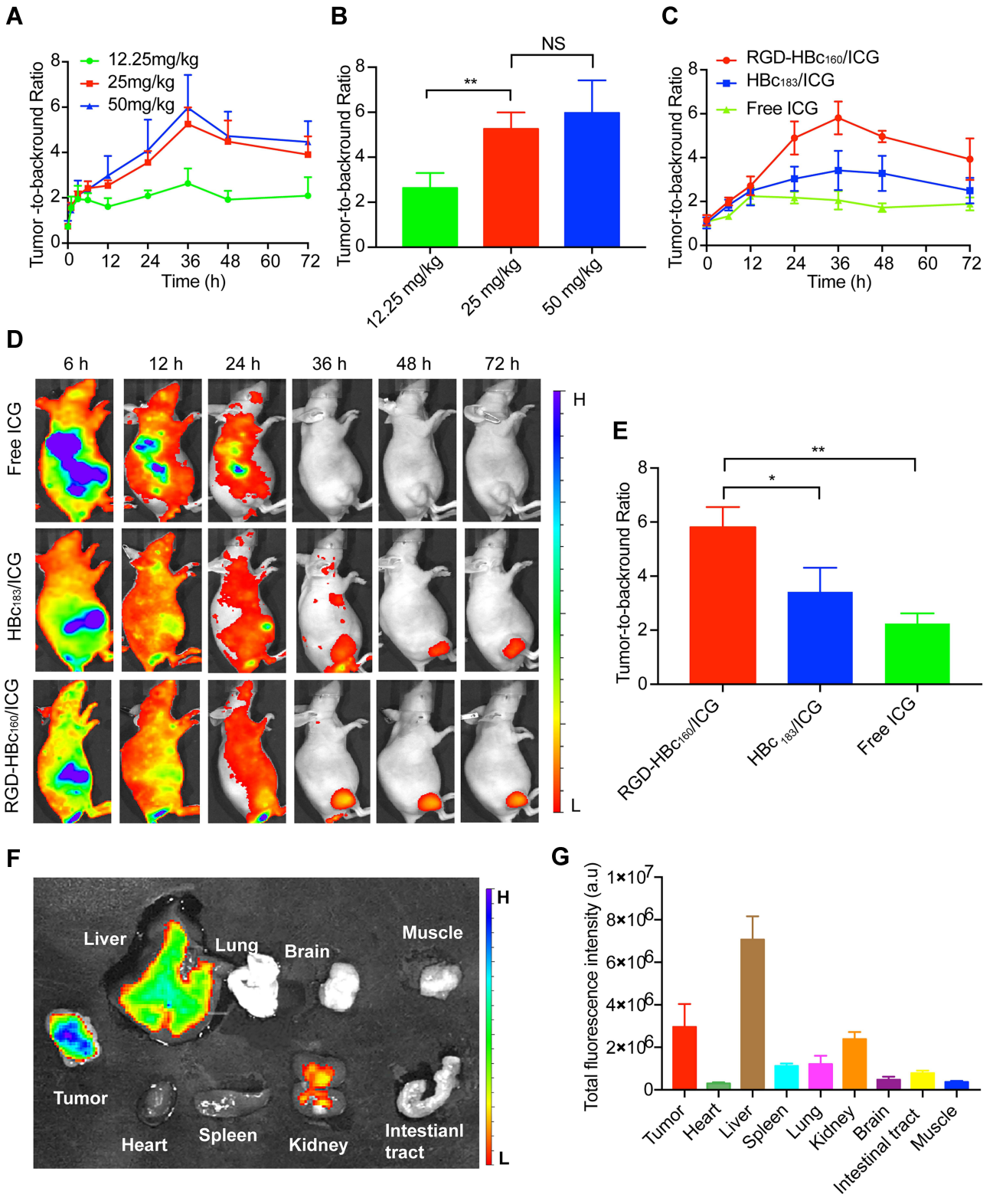

Figure 2 Validation of the target specificity of RGD-HBc$_{160}$/ICG in subcutaneous breast cancer tumor models. (**A**) Representative quantification of TBR in MDA-MAB-231 tumor mice as a function of time after intravenous injection with different doses of RGD-HBc$_{160}$/ICG and comparison of TBR at 36 h time points (**B**). (**C**) Representative quantification of TBR in MDA-MAB-231 tumor mice as a function of time after intravenous injection with RGD-HBc$_{160}$/ICG, HBc$_{183}$/ICG, ICG, and the Fluorescence images of mice (**D**). (**E**) Comparison of specific binding with RGD-HBc$_{160}$/ICG compared with HBc$_{183}$/ICG and the free ICG at maximum TBR (right). (**F**) Fluorescence images from organs and tumors excised at 36 h after injection of RGD-HBc$_{160}$/ICG, and semi-quantitative analysis of total fluorescence intensity from the samples (**G**). *P<0.05, **P<0.01.

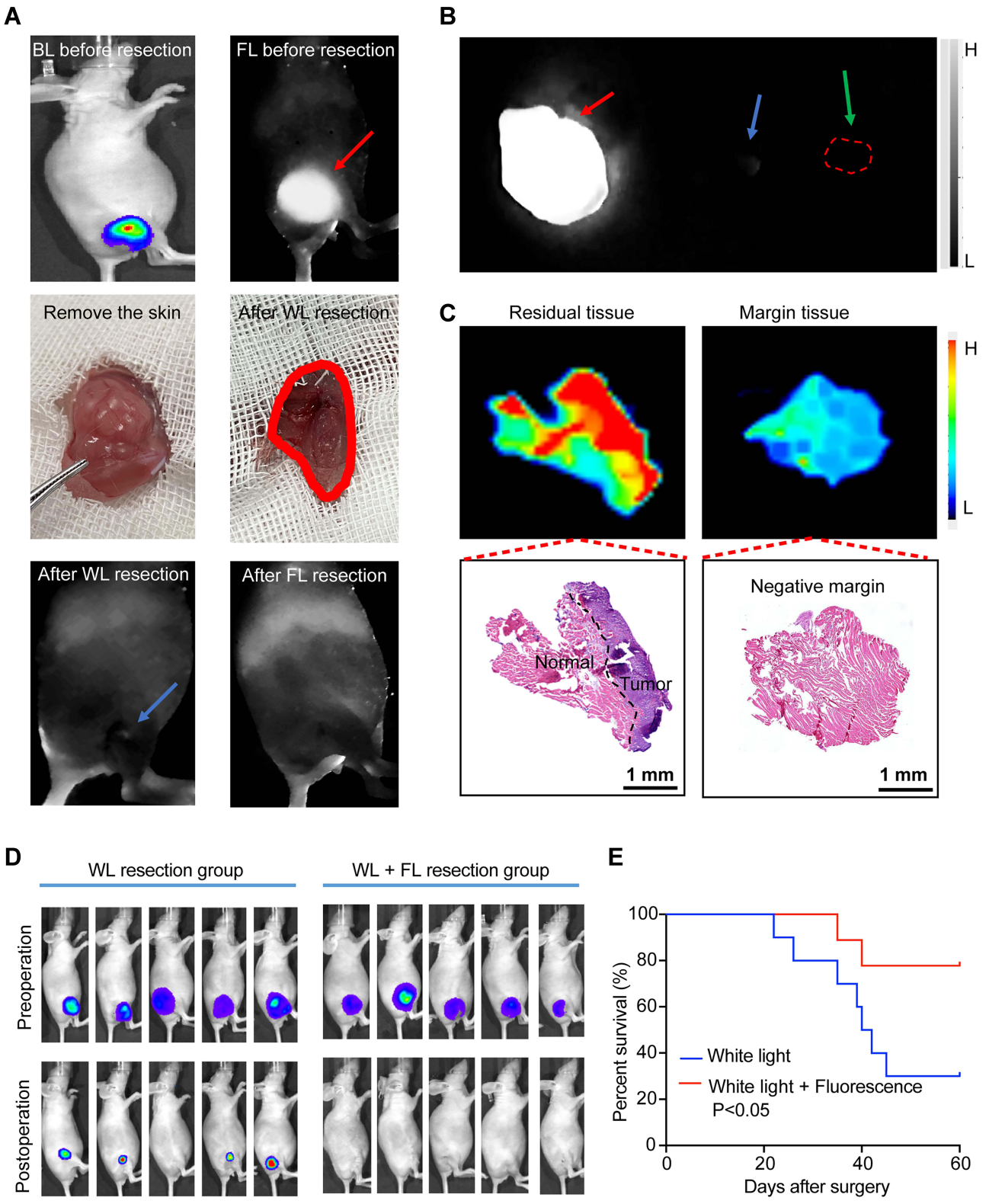

Figure 3 Fluorescent imaging-guided surgical resections of infiltrative MDA-MB-231-luc tumors. (**A**) The procedure of tumor resection in represented mice guided by white light (WL) plus fluorescence imaging (FL) (blue arrow, residual fluorescence signal in the surgery bed). (**B**) Ex-*vivo* fluorescence imaging of excised tissue (red arrow, primary tumor excised under white light only; blue arrow, residual tumor tissue; green arrow, negative surgical margins). (**C**) Fluorescence image, upper, and H/E stain, lower, for residual tumor tissue and negative margins. (**D**) Representative preoperative and postoperative bioluminescence images following white light surgery only (n = 10) and white light plus fluorescence-guided surgery (n = 10) with Kaplan-Meier survival analysis of two groups (**E**).

Fluorescence Guided Surgical Resection in Mammary Tumor Transgenic Mice

To assess the feasibility of RGD-HBc_{160}/ICG based fluorescence imaging-guided tumor resection in a transgenic mouse model, breast tumors were sequentially resected from MMTV-PyVT mice after injection of RGD-HBc_{160}/ICG. The MMTV-PyVT model provided representative examples of breast cancers with positive resection margins (Figure 4A), while the wild type models provided examples of negative resection margins (Figure 4B). In both groups, intraoperative imaging-guided with step-wise resection was successfully performed. Quantitatively, the in vivo MFI was 10.6 ± 6.9 in MMTV-PyVT tissue segments and was significantly higher than the MFI in the wild-type mouse tissues (3.9 ± 2.0) ($P<0.05$) (Figure 4C). The α_v expression in the MMTV-PyVT breast tumor segments was also higher than that of the wild-type breast segments (IHC score 6.7 ± 0.7 vs 2.7 ± 0.9, $P<0.05$) (Figure 4D).

Subsequently, due to transgenic mice at different pathological stages, fluorescence intensity in the tissues was compared with pathological diagnosis and the ROC curves were plotted to evaluate the diagnostic accuracy of fluorescence imaging at various imaging signal thresholds. The area under the curve (AUC) for differentiation between malignant and benign tissues by fluorescence was 0.846 (95% confidence interval [CI]: 0.74, 0.96) (Figure 5A). At the same time, quantitative fluorescence analysis comparing different pathological tissue types in the microscopic sections showed that the fluorescence signal in invasive carcinoma tissues was the strongest. Carcinoma in situ had a medium signal, and fat and normal breast tissues had low signals (Figure 5B), again suggesting the ability of the RGD-HBc_{160}/ICG probe to aggregate specifically in breast cancer tissues. To highlight the potential for clinical translation, signaling provided by the RGD-HBc_{160}/ICG probe permitted successful distinction between invasive ductal carcinoma and normal mammary duct tissue at the microscopic level, and signal intensity and tumor status corresponded well to α_v expression (Figure 5C).

Immunogenic Response of RGD-HBc_{160} in Mice

As shown in Figure 6A and B, mice in RGD-HBc_{160} group showed significantly decreased $CD3^+$ $CD8^+$ T cells in spleen tissues than the HBc_{183} group ($P<0.01$), there was no significant difference in $CD3^+$ $CD4^+$ T cells between the two groups. To further checked the cytokine levels in serum after the treatments, the ELISA results showed that serum obtained from the immunized mice induced a higher concentration of the γ-IFN and TNF-α in HBc_{183} than RGD-HBc_{160} group ($P<0.01$), whereas these was low level in the non-immunized group (Figure 6C and D). To assess the humoral immune response induced by RGD-HBc_{160}, we performed the semi-quantitative ELISA assays to compare the relative concentration of anti-RGD-HBc_{160} and anti-HBc_{183} antibodies in the serum. As shown in Figure 6E, the concentration of antibody in RGD-HBc_{160}-immunized mice lower than HBc_{183}-immunized mice (1.1 ± 0.1 vs 0.63 ± 0.2, $P<0.01$).

In-Vivo Safety Evaluation

The biosafety of the probe was checked in immunocompetent BALB/c mice. Body weights over the course of the study remained normal growth trend (Figure S6A), suggesting that RGD-HBc_{160}/ICG was not toxic to the mice. The ALT, AST, Cre, and Urea levels increased at 1 h after injection of the probe and returned to normal after 7 days (Figure S6B). In addition, hemocytology indexes (RBC, WBC, PLT, lymphocyte) conducted on day 1, day 7, and day 21 post-injection changes within the normal range (Figure S6C). Histopathologic analysis of major organs with H/E stain showed no obvious pathologic changes (Figure S6D).

Expression of α_v in Human Breast Tissues

α_v expression was measured in breast cancer neovasculature, epithelium, and stroma in human breast cancer (n = 40) and in the corresponding paracancerous tissues (n = 40). α_v was expressed in 85% of the cancers (34/40) and 60% of the paracancerous tissues (24/40) (Table S1). Among all the breast cancer tissues, 9 cancer tissues were Luminal A type, 18 cancer tissues were Luminal B type, 9 cancer tissues were HER2 positive type, 4 cancer tissues were triple negative breast cancer (TNBC) type. Overall, α_v expression was higher in breast cancer tissues compared to paracancerous tissues, and the IHC score of the cancer tissues was about 2-fold higher than the IHC score of the paracancerous tissues ($P<0.001$) (Figure S7A and B).

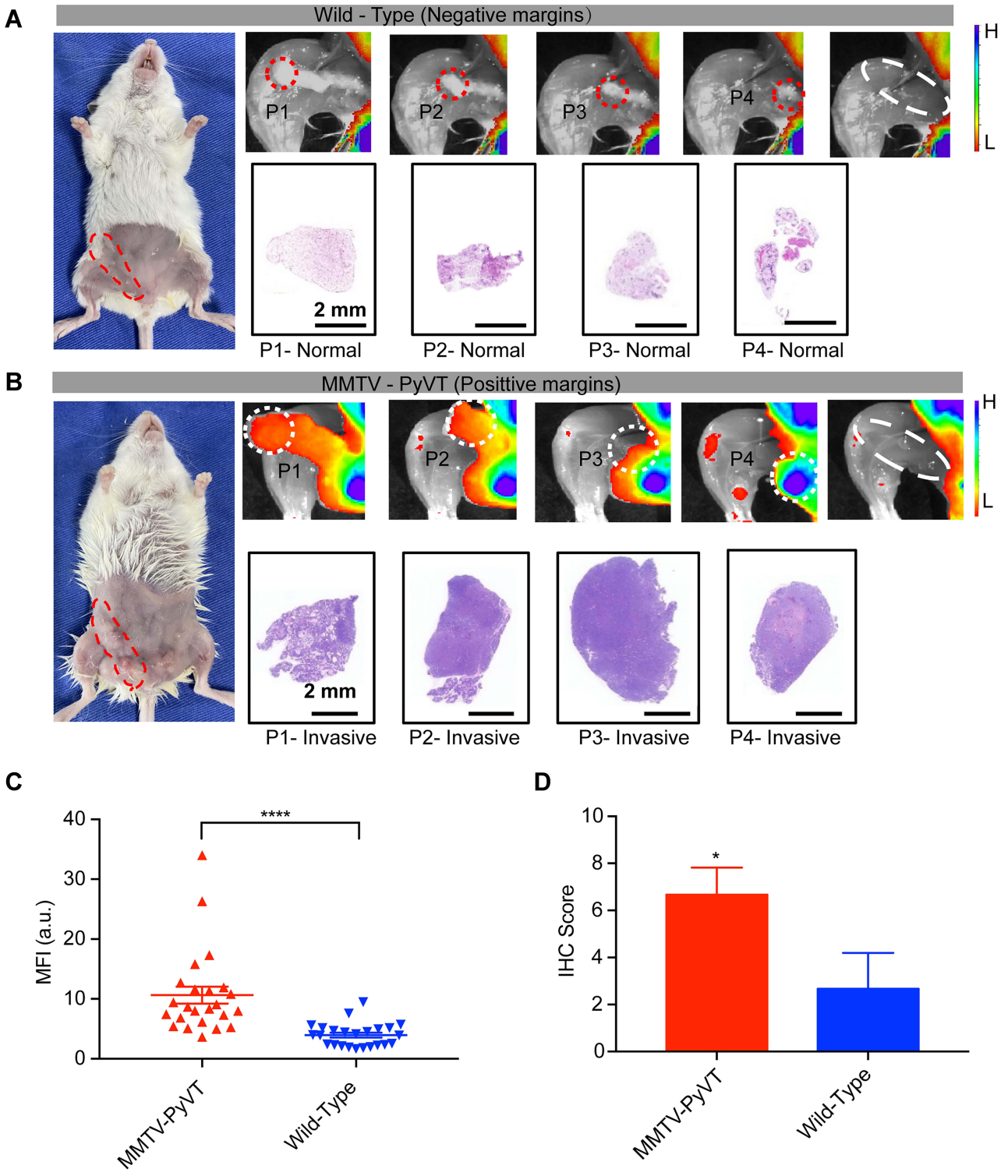

Figure 4 Fluorescence imaging-guided surgical resection in a mammary tumor transgenic model. (**A**) Simulated negative surgical margins in fluorescence images of combined fourth and fifth mammary glands from an 8-week-old wild-type female mouse. The tissue to be resected is highlighted with a dashed circle. The second row shows representative histological staining of resected portions (P1-4). (**B**) Simulated positive surgical margins in fluorescence images of combined fourth and fifth mammary glands from an 8-week-old MMTV-PyVT female mouse following the same excision sequence as above. (**C**) Representative mean fluorescence intensity of tissues with positive and negative surgical margins pooled from the 6 mice. (**D**) Representation of immunohistochemistry scores for α_v-stained breast tissues from MMTV-PyVT and wild-type mice. *P<0.05, ****P<0.0001.

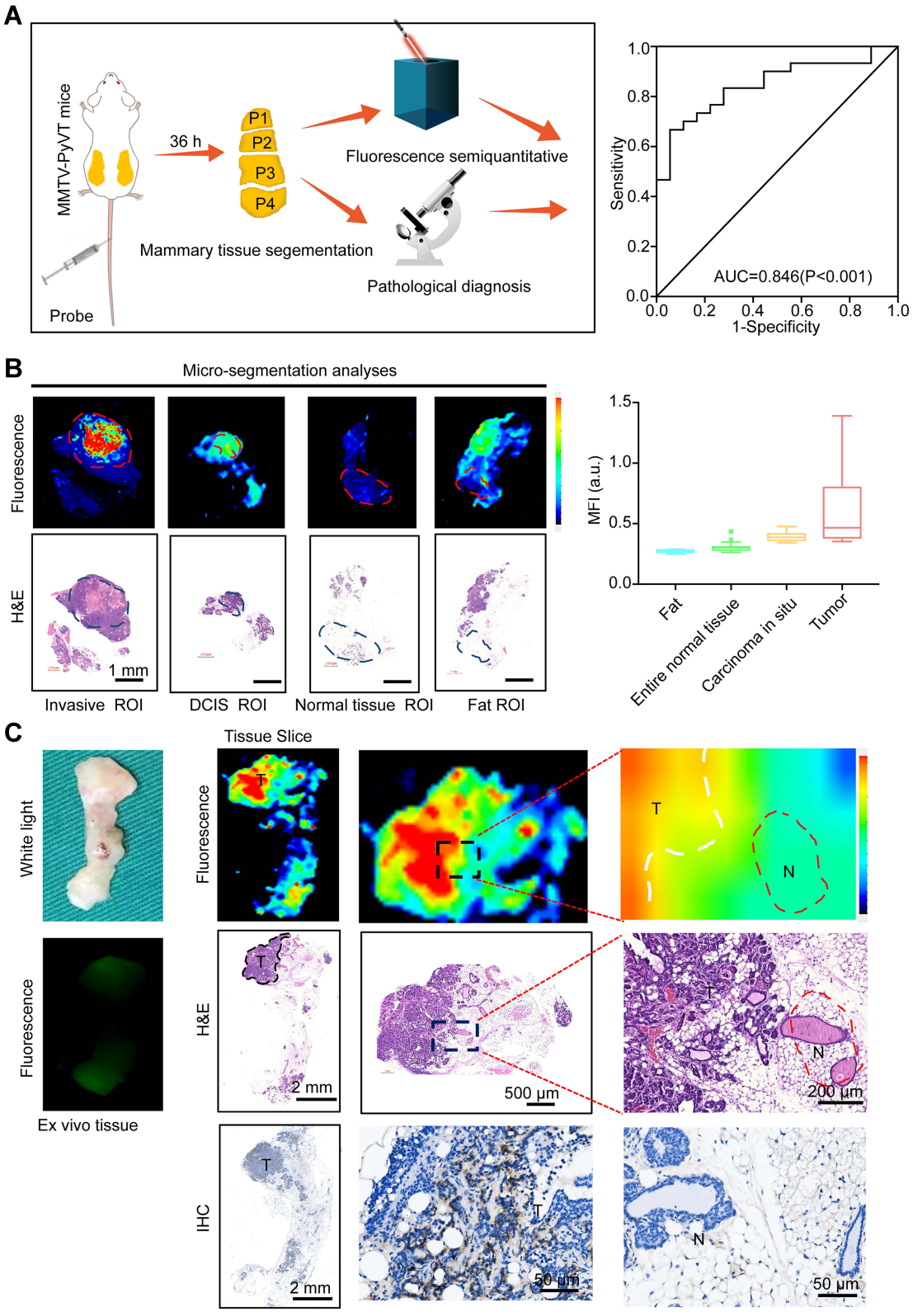

Figure 5 Distribution of the fluorescent probe in the transgenic mouse mammary gland. (**A**) Schematic illustration of the performance evaluation (left) and the receiver operating characteristic (ROC) curve of fluorescence imaging to differentiate between normal tissues and cancer (right). (**B**) Microscopic bio-distribution of RGD-HBc_{160}/ICG in breast tissues based on micro-segmentation analyses (left). The upper row shows a representative example of the fluorescence ROI per tissue type based on H/E staining. The lower row shows the corresponding H/E staining image. MFI of all per-tissue type ROIs are shown in the right panel. (**C**) Ex vivo fluorescent imaging of breast tissue showing corresponding fluorescence intensity (upper), H/E sections (middle), and immunohistochemical stain of α_v expression (lower).

https://doi.org/10.2147/IJN.S343479 DovePress

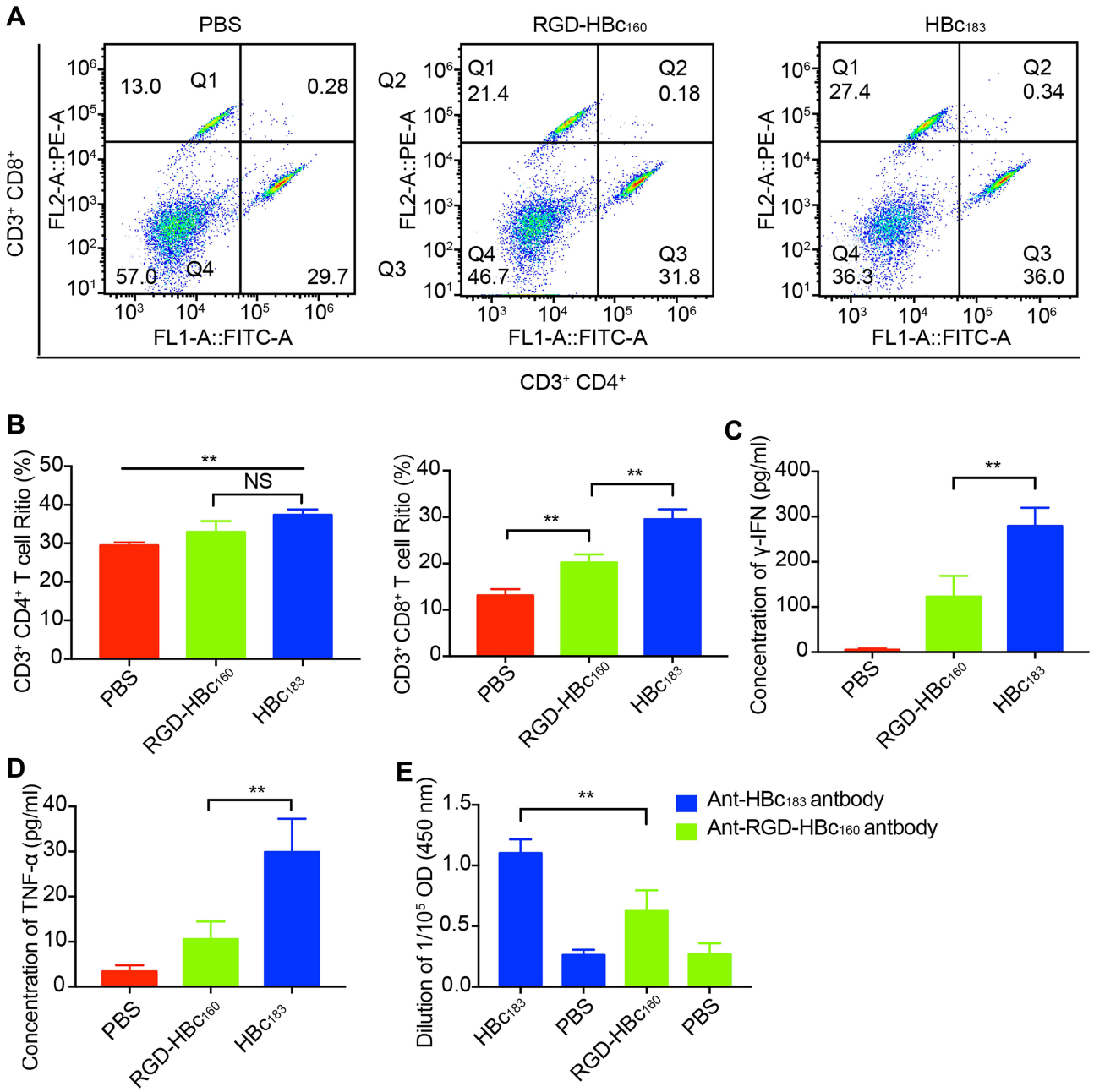

Figure 6 RGD-HBc$_{160}$ induced immune responses in BALB/c mice. (**A**) Flow cytometry determination of Ths (CD3$^+$ CD4$^+$) and CTLs (CD3$^+$ CD8$^+$) in the spleen tissue from each group, (**B**) Quantitative analysis of the means between the different groups. Comparison of the level of serum γ-IFN(**C**) and TNF-α (**D**) from RGD-HBc$_{160}$-immunized, HBc$_{183}$-immunized, and non-immunized mice. (**E**) Comparison of the corresponding serum antibody levels from each group on 7 days after the second immunization. **P<0.01.

Discussion

Fluorescence-guided surgery has been shown to increase the tumor-detection rate, reduce the rate of positive margins, and improve outcomes by enhancing intraoperative tumor visualization in a variety of cases.[11,29,30] Several previous studies have reported that HBc VLP can play an excellent role in tumor delivery, such as loading with the chemotherapy drugs for melanoma treatment,[31] loading with photosensitizer for photoacoustic imaging in glioma mouse model.[25,32] Herein, we demonstrated the novel use of the HBc VLPs-based NIR probe as a tool to delineate tumor margin in fluorescence-guided surgery. In comparison with the free ICG, RGD-HBc$_{160}$/ICG achieved a longer tumor retention time

and TBR was significantly enhanced (~5.8) with background signals reduced in this special time window, resulting in the discrimination between cancer and normal tissue which avoids incomplete resections.

Among the various targeted NIR probes with potential for clinical translation, most delivery systems have been based on commercial monoclonal antibodies.[33,34] For example, the VEGF-A targeting bio-conjugate bevacizumab-IRDye800CW has progressed into clinical trials (Phase II) for guiding breast-conserving surgery.[35] However, it should be noted that monoclonal antibodies are less efficient at loading drugs, with an antibody/dye ratio of <1:10. Furthermore, monoclonal antibodies and the corresponding covalently bonded fluorescent dyes, such as IRDye800CW-NHS, ICG-NHS, are relatively expensive to prepare and not approved by the FDA. In this study, we adopted a natural protein-based nanoparticle, the structure of which can be tailored to obtain targeting capacity. Such a nanoparticle can have multiple binding sites on its surface and can load much more fluorescent dyes (antibody/dye mole ratio >1:300). What's more, RGD-HBc_{160} VLPs can be produced by various prokaryotic expression systems, and ICG can be encapsulated into the VLPs through disassembly/reassembly rather than covalent binding, both of which can significantly reduce costs. Tumor-targeted peptides, aptamers, or small molecule-drugs have also been adopted as carriers for the delivery of dyes. However, these small molecule ligands can be metabolized rapidly, resulting in a short time window for imaging (<12 h).[36,37] In our study, RGD-HBc_{160} monomers could self-assemble as VLP nanoparticles that were generally stable over a wide range of the in vivo environment[38] and could achieve the long-time tumor retention in-vivo (imaging time window >24 h). Moreover, the RGD peptide sequence was integrated into the surface of HBc protein through genetic engineering technology, which could further overcome the shortcomings of the traditional polypeptide surface modification, such as easy hydrolysis and instability.

The subcutaneous xenograft mouse model has often been the sole model used in preclinical studies on fluorescence-guided tumor resection. However, this model cannot fully simulate the intraoperative condition. To more accurately simulate the intraoperative situation, the establishment of an infiltrative-tumor model can be better used to evaluate molecular probes.[39] In the present study, the infiltrative tumor model was used to replicate the difficulty of margin visualization under white light, and 80% (8/10) of the mice had residual tumor after white-light only surgery, while fluorescence imaging-guided surgery reduced the margin positive rate to 20% (2/10). In addition, as a perfect analog of human breast cancer, a well-characterized transgenic mouse model of breast cancer development, was used in this study, which can spontaneously progress to breast cancer through distinct pathological stages: normal breast tissue, hyperplasia, DCIS, and invasive breast cancer.[40] Based on this particular animal model, we designed ingenious experiments that showed the excellent NIR fluorescence imaging capability to differentiate between benign and malignant breast tissues, and the multi-level framework analysis also showed that the fluorescence signal, histological diagnosis, and integrin expression had strong correlation.

Some inorganic or synthetic nano-carriers have caused concern because of retention and accumulation in the body post-imaging, due to potential toxic responses and immunogenicity. HBc VLPs contains natural protein, with the advantages of good biodegradability and compatibility, and have been applied in the development of vaccines, showing good safety.[41,42] However, there are multiple immune epitopes in HBc VLP, which can easily stimulate the immune response of the body. In the present study, MIR of HBc protein was mutated by the RGD sequence. And compared with previously reported RGD-HBc_{183} VLP,[25] the amino acids in B cell and CTL epitope of RGD-HBc_{160} were partial substituted, and the redundant amino acids on the C-terminus which is not related to the structure assembly were eliminated. We further investigated the immunology of the protein in vivo, the results showed that the cellular and humoral responses induced by RGD-HBc_{160} were decreased than those induced by wild-type HBc_{183}. Furthermore, a pilot toxicology study was performed and result showed that the probe was well tolerated. Although there were insignificantly changes in blood bioChemistry panels immediately after injection, and these levels were back within the normal range after one week, larger toxicology studies experiment need to be performed to determine the meaning of these changes before conclusions can be drawn.

There are some limitations to this study. First, in this study, 2 mice in the fluorescent imaging-guided resection group still had a residual tumor, which might be explained by the poor penetration that is an inherent defect of traditional NIR fluorescent imaging (<1000 nm). Thus, in the future, fluorescence imaging combined with photoacoustic imaging or extended to the NIR-II window (1000 to 1700 nm) may achieve even greater penetration and sensitivity.[43,44] Secord, the

feasibility and safety of RGD-HBc_{160}/ICG were evaluated only at the small animal level in this study. To accelerate clinical transformation, further studies in large animals are necessary.

The results of our study suggest that the RGD-HBc_{160}/ICG fluorescent probe allows specific targeting of breast cancers. The probe performed well in delineating tumor boundaries and assessing the pathological status of tissues in mouse models. Add its biocompatibility, biodegradation, low toxicity, and low immunogenicity, and the RGD-HBc_{160}/ICG has clinical translation potential as an effective tool to aid surgeons in real-time tumor resection during BCS.

Data Accessibility Statement

The original contributions presented in the study are included in the article/Supplementary Material. Further inquiries can be directed to the corresponding authors.

Ethics Statement

All animal work was approved by the ethics committee of Xiamen University and was conducted in accordance with the principles of the Association for Assessment and Accreditation of Laboratory Animal Care International (AAALAC). The procedures used in this study also adhere to the tenets of the Declaration of Helsinki.

Acknowledgments

The present study was supported by the National Natural Science Foundation of China (Grant No. 91859120, No. U1904206, No. 32171363), Natural Science Foundation of Fujian Province of China (No. 2020J01015), and the Fujian Major Scientific and Technological Special Project for Social Development (No. 2020YZ016002).

Disclosure

The authors report no conflicts of interest in this work.

References

1. Sung H, Ferlay J, Siegel RL, et al. Global cancer statistics 2020: GLOBOCAN estimates of incidence and mortality worldwide for 36 cancers in 185 countries. *CA Cancer J Clin*. 2021;71(3):209–249. doi:10.3322/caac.21660
2. Fisher B, Anderson S, Bryant J, et al. Twenty-year follow-up of a randomized trial comparing total mastectomy, lumpectomy, and lumpectomy plus irradiation for the treatment of invasive breast cancer. *N Engl J Med*. 2002;347(16):1233–1241. doi:10.1056/NEJMoa022152
3. Waljee JF, Hu ES, Newman LA, Alderman AK. Predictors of re-excision among women undergoing breast-conserving surgery for cancer. *Ann Surg Oncol*. 2008;15(5):1297–1303. doi:10.1245/s10434-007-9777-x
4. Biglia N, Maggiorotto F, Liberale V, et al. Clinical-pathologic features, long term-outcome and surgical treatment in a large series of patients with invasive lobular carcinoma (ILC) and invasive ductal carcinoma (IDC). *Eur J Surg Oncol*. 2013;39:455–460.
5. Tipirneni KE, Warram JM, Moore LS, et al. Oncologic procedures amenable to fluorescence-guided surgery. *Ann Surg*. 2017;266(1):36–47. doi:10.1097/SLA.0000000000002127
6. St John ER, Al-Khudairi R, Ashrafian H, et al. Diagnostic accuracy of intraoperative techniques for margin assessment in breast cancer surgery: a meta-analysis. *Ann Surg*. 2017;265(2):300–310. doi:10.1097/SLA.0000000000001897
7. Tummers WS, Warram JM, Tipirneni KE, et al. Regulatory aspects of optical methods and exogenous targets for cancer detection. *Cancer Res*. 2017;77(9):2197–2206. doi:10.1158/0008-5472.CAN-16-3217
8. Ogawa M, Takakura H. In vivo molecular imaging for biomedical analysis and therapies. *Anal Sci*. 2018;34(3):273–281. doi:10.2116/analsci.34.273
9. Hernot S, van Manen L, Debie P, Mieog JSD, Vahrmeijer AL. Latest developments in molecular tracers for fluorescence image-guided cancer surgery. *Lancet Oncol*. 2019;20(7):e354–e367. doi:10.1016/S1470-2045(19)30317-1
10. Wen Y, Huo F, Yin C. Organelle targetable fluorescent probes for hydrogen peroxide. *Chin Chem Lett*. 2019;30(10):1834–1842. doi:10.1016/j.cclet.2019.07.006
11. Chi C, Du Y, Ye J, et al. Intraoperative imaging-guided cancer surgery: from current fluorescence molecular imaging methods to future multi-modality imaging technology. *Theranostics*. 2014;4(11):1072–1084. doi:10.7150/thno.9899
12. Luo X, Li J, Zhao J, Gu L, Qian X, Yang Y. A general approach to the design of high-performance near-infrared (NIR) D-p-A type fluorescent dyes. *Chin Chem Lett*. 2019;30(4):839–846. doi:10.1016/j.cclet.2019.03.012
13. Yamada Y, Ohno M, Fujino A, et al. Fluorescence-guided surgery for hepatoblastoma with indocyanine green. *Cancers*. 2019;11(8):1215. doi:10.3390/cancers11081215
14. Jung SY, Han JH, Park SJ, et al. The sentinel lymph node biopsy using indocyanine green fluorescence plus radioisotope method compared with the radioisotope-only method for breast cancer patients after neoadjuvant chemotherapy: a prospective, randomized, open-label, single-center phase 2 trial. *Ann Surg Oncol*. 2019;26(8):2409–2416. doi:10.1245/s10434-019-07400-0

15. Backes FJ, Cohen D, Salani R, et al. Prospective clinical trial of robotic sentinel lymph node assessment with isosulfane blue (ISB) and indocyanine green (ICG) in endometrial cancer and the impact of ultrastaging (NCT01818739). *Gynecol Oncol*. 2019;153(3):496–499. doi:10.1016/j.ygyno.2019.03.252
16. Kessous R, How J, Abitbol J, et al. Triple tracer (blue dye, indocyanine green, and Tc99) compared to double tracer (indocyanine green and Tc99) for sentinel lymph node detection in endometrial cancer: a prospective study with random assignment. *Int J Gynecol Cancer*. 2019;29(7):1121–1125. doi:10.1136/ijgc-2019-000387
17. Diep GK, Hui JY, Marmor S, et al. Postmastectomy reconstruction outcomes after intraoperative evaluation with indocyanine green angiography versus clinical assessment. *Ann Surg Oncol*. 2016;23(12):4080–4085. doi:10.1245/s10434-016-5466-y
18. Choi HS, Nasr K, Alyabyev S, et al. Synthesis and in vivo fate of zwitterionic near-infrared fluorophores. *Angew Chem Int Ed Engl*. 2011;50(28):6258–6263. doi:10.1002/anie.201102459
19. Keating J, Tchou J, Okusanya O, et al. Identification of breast cancer margins using intraoperative near-infrared imaging. *J Surg Oncol*. 2016;113(5):508–514. doi:10.1002/jso.24167
20. Langer R. New methods of drug delivery. *Science*. 1990;249(4976):1527–1533. doi:10.1126/science.2218494
21. James ND, Coker RJ, Tomlinson D, et al. Liposomal doxorubicin (Doxil): an effective new treatment for Kaposi's sarcoma in AIDS. *Clin Oncol*. 1994;6(5):294–296. doi:10.1016/S0936-6555(05)80269-9
22. Green MR, Manikhas GM, Orlov S, et al. Abraxane, a novel Cremophor-free, albumin-bound particle form of paclitaxel for the treatment of advanced non-small-cell lung cancer. *Ann Oncol*. 2006;17(8):1263–1268. doi:10.1093/annonc/mdl104
23. Burgess P, Hutt PB, Farokhzad OC, Langer R, Minick S, Zale S. On firm ground: IP protection of therapeutic nanoparticles. *Nat Biotechnol*. 2010;28(12):1267–1270. doi:10.1038/nbt.1725
24. Lu Y, Chan W, Ko BY, VanLang CC, Swartz JR. Assessing sequence plasticity of a virus-like nanoparticle by evolution toward a versatile scaffold for vaccines and drug delivery. *Proc Natl Acad Sci USA*. 2015;112(40):12360–12365. doi:10.1073/pnas.1510533112
25. Shan W, Chen R, Zhang Q, et al. Improved stable Indocyanine Green (ICG)-mediated cancer optotheranostics with naturalized Hepatitis B core particles. *Adv Mater*. 2018;30(28):e1707567. doi:10.1002/adma.201707567
26. Pumpens P, Grens E. Hepatitis B core particles as a universal display model: a structure-function basis for development. *FEBS Lett*. 1999;442(1):1–6. doi:10.1016/S0014-5793(98)01599-3
27. Li D, Zhang J, Chi C, et al. First-in-human study of PET and optical dual-modality image-guided surgery in glioblastoma using Ga-IRDye800CW-BBN. *Theranostics*. 2018;8:2508–2520. doi:10.7150/thno.25599
28. Yang F, Liu S, Liu X, et al. In vivo visualization of tumor antigen-containing microparticles generated in fluorescent-protein-elicited immunity. *Theranostics*. 2016;6(9):1453–1466. doi:10.7150/thno.14145
29. Chen QY, Xie JW, Zhong Q, et al. Safety and efficacy of indocyanine green tracer-guided lymph node dissection during laparoscopic radical gastrectomy in patients with gastric cancer: a randomized clinical trial. *JAMA Surg*. 2020;155(4):300–311. doi:10.1001/jamasurg.2019.6033
30. Stummer W, Pichlmeier U, Meinel T, et al. Fluorescence-guided surgery with 5-aminolevulinic acid for resection of malignant glioma: a randomised controlled multicentre Phase III trial. *Lancet Oncol*. 2006;7(5):392–401. doi:10.1016/S1470-2045(06)70665-9
31. Shan W, Zhang D, Wu Y, et al. Modularized peptides modified HBc virus-like particles for encapsulation and tumor-targeted delivery of doxorubicin. *Nanomedicine*. 2018;14(3):725–734. doi:10.1016/j.nano.2017.12.002
32. Liu Y, Liu H, Yan H, et al. Aggregation-induced absorption enhancement for deep near-infrared ii photoacoustic imaging of brain gliomas in vivo. *Adv Sci*. 2019;6:1801615.
33. Lamberts LE, Koch M, de Jong JS, et al. Tumor-specific uptake of fluorescent Bevacizumab-IRDye800CW microdosing in patients with primary breast cancer: a Phase I feasibility study. *Clin Cancer Res*. 2017;23(11):2730–2741. doi:10.1158/1078-0432.CCR-16-0437
34. Kularatne SA, Thomas M, Myers CH, et al. Evaluation of novel prostate-specific membrane antigen-targeted near-infrared imaging agent for fluorescence-guided surgery of prostate cancer. *Clin Cancer Res*. 2019;25(1):177–187. doi:10.1158/1078-0432.CCR-18-0803
35. Koller M, Qiu SQ, Linssen MD, et al. Implementation and benchmarking of a novel analytical framework to clinically evaluate tumor-specific fluorescent tracers. *Nat Commun*. 2018;9(1):3739. doi:10.1038/s41467-018-05727-y
36. Jones JE, Busi SB, Mitchem JB, Amos-Landgraf JM, Lewis MR. Evaluation of a tumor-targeting, near-infrared fluorescent peptide for early detection and endoscopic resection of polyps in a rat model of colorectal cancer. *Mol Imaging*. 2018;17:1536012118790065. doi:10.1177/1536012118790065
37. Hoogstins CE, Tummers QR, Gaarenstroom KN, et al. A novel tumor-specific agent for intraoperative near-infrared fluorescence imaging: a translational study in healthy volunteers and patients with ovarian cancer. *Clin Cancer Res*. 2016;22(1):2929–2938. doi:10.1158/1078-0432.CCR-15-2640
38. Ausar SF, Foubert TR, Hudson MH, Vedvick TS, Middaugh CR. Conformational stability and disassembly of Norwalk virus-like particles. Effect of pH and temperature. *J Biol Chem*. 2006;281(28):19478–19488. doi:10.1074/jbc.M603313200
39. Zhang M, Kobayashi N, Zettlitz KA, et al. Near-infrared dye-labeled anti-prostate stem cell antigen minibody enables real-time fluorescence imaging and targeted surgery in translational mouse models. *Clin Cancer Res*. 2019;25(1):188–200. doi:10.1158/1078-0432.CCR-18-1382
40. Wilson KE, Bachawal SV, Willmann JK. Intraoperative resection guidance with photoacoustic and fluorescence molecular imaging using an anti-B7-H3 antibody-indocyanine green dual contrast agent. *Clin Cancer Res*. 2018;24(15):3572–3582. doi:10.1158/1078-0432.CCR-18-0417
41. Zhang J, Zhang XF, Huang SJ, et al. Long-term efficacy of a hepatitis E vaccine. *N Engl J Med*. 2015;372(10):914–922. doi:10.1056/NEJMoa1406011
42. Liaw YF, Chu CM. Hepatitis B virus infection. *Lancet*. 2009;373(9663):582–592. doi:10.1016/S0140-6736(09)60207-5
43. Carr JA, Franke D, Caram JR, et al. Shortwave infrared fluorescence imaging with the clinically approved near-infrared dye indocyanine green. *Proc Natl Acad Sci U S A*. 2018;115(17):4465–4470. doi:10.1073/pnas.1718917115
44. Yao J, Kaberniuk AA, Li L, et al. Multiscale photoacoustic tomography using reversibly switchable bacterial phytochrome as a near-infrared photochromic probe. *Nat Methods*. 2016;13(1):67–73. doi:10.1038/nmeth.3656